Thin Solid Films 825 (2025) 140744

Contents lists available at ScienceDirect

Thin Solid Films

journal homepage: www.elsevier.com/locate/tsf

Resolving the microstructure of aluminum-doped zinc oxide thin films grown on different silicon heterojunction solar cell structures by advanced transmission electron microscopy

Sara Alkhereibi [a,b,d,*], Muhammad Ainul Yaqin [b,c], Alexander Eberst [b,c], Binbin Xu [b,c], Janghyun Jo [a], Husain Alsamamra [e], Andreas Lambertz [b], Uwe Rau [b,c], Kaining Ding [b], Joachim Mayer [a]

[a] *Ernst Ruska-Centre for Microscopy and Spectroscopy with Electrons, Forschungszentrum Jülich GmbH, Jülich 52425, Germany*
[b] *Institute for Energy Materials and Devices - Photovoltaik, Forschungszentrum Jülich GmbH, Jülich 52425, Germany*
[c] *Jülich-Aachen Research Alliance (JARA-Energy) and Faculty of Electrical Engineering and Information Technology, RWTH Aachen University, Schinkelstr. 2, Aachen 52062, Germany*
[d] *Faculty of Mathematics, Computer Science and Natural Sciences, RWTH Aachen University, Aachen 52062, Germany*
[e] *Department of Physics, Al-Quds University, Jerusalem 20002, Palestine*

ARTICLE INFO

Keywords:
Transmission electron microscopy
Precession-assisted four-dimensional scanning transmission electron microscopy
Phase and orientation mapping
Silicon heterojunction
Transparent conductive oxide

ABSTRACT

Advanced microscopy techniques have been employed to resolve the microstructure of transparent conductive oxide (TCO) contacts in silicon heterojunction solar cells. Aluminum-doped zinc oxide (AZO) stands out as a TCO material because of its low cost, abundance, and good optoelectrical properties. The polycrystalline AZO thin films have yielded promising results in solar cell design. However, understanding the nanostructure of AZO thin-film materials is vital for enhancing the cell performance by focusing on the formation of large grains and their influence on the charge-carrier mobility of the film. Therefore, we employed high-resolution transmission electron microscopy (HRTEM) and precession-assisted four-dimensional scanning transmission electron microscopy (4D-STEM) with an automated crystal orientation analysis. These techniques can be used to determine the grain sizes of AZO films sputtered on hydrogenated amorphous silicon (a-Si:H) and hydrogenated nanocrystalline silicon (nc-Si:H) layers. Columnar grains in the AZO/a-Si:H film are evident in the grain mapping with diameters greater than 10 nm, whereas in the AZO/nc-Si:H film, the grains begin at diameters less than 10 nm, showing smaller grains near the substrate than at the top of the film. Additionally, the double-layer with indium-thin doped oxide (ITO)/AZO stack started with grain diameters varying from 5 to 90 nm. They exhibit significantly larger and irregular boundaries. Therefore, microstructural characterization showed that larger columnar grains might lead to higher mobility in the AZO layer. This finding indicates that the impact of the ITO seed layer on AZO significantly enhances grain size, improves charge carrier mobility, and overall improves the power conversion efficiency (η) to be 23.6% comparable to those of AZO on a-Si:H and nc-Si:H.

1. Introduction

The common goal in solar cell technology is to increase the power conversion efficiency (η) of solar cells. Most photovoltaic research focuses on improving the performance of innovative materials and reducing manufacturing costs. To date, crystalline silicon solar cells have remained dominant in the photovoltaic market, accounting for approximately 97 % of the global production of solar cells and modules [1]. So far, silicon heterojunction solar (SHJ) cells using transparent conductive oxide (TCO) materials have achieved a record power conversion efficiency of up to 26.81 % [2,3]. TCOs are commonly utilized as electrode contacts on both sides of SHJ solar cells, owing to their appealing physical properties. The TCO provides lateral conduction for charge carrier collection and acts as anti-reflective coating [4]. For efficient solar cell performance, TCOs must possess high optical transparency and electrical conductivity [5]. For instance, tin-doped indium oxide (SnO_2: In_2O_3, ITO), Tungsten doped indium oxide (In_2O_3: W, IWO) [6] and aluminum-doped zinc oxide (Al_2O_3: ZnO, AZO) are among the

---

[*] Corresponding author.
E-mail address: s.alkhereibi@fz-juelich.de (S. Alkhereibi).

https://doi.org/10.1016/j.tsf.2025.140744
Received 31 October 2024; Received in revised form 14 July 2025; Accepted 14 July 2025

high-performance TCO materials. These materials are polycrystalline materials consisting of small crystalline grains separated by grain boundaries, offering potential advantages in terms of stability and transparency for different photovoltaic applications.

AZO has been extensively studied for many years [7,8] because it is a promising alternative to In_2O_3-based TCO films, which have better optoelectrical properties but are more expensive and require rare materials such as indium. Despite AZO's potential as a cost-effective and abundant material, its performance trails behind that of ITO for some reasons: on the one hand, the initial crystallinity of AZO films near the substrate is often suboptimal, resulting in high resistivity or even insulation in this region, necessitating the use of appropriate seed layers to enhance crystalline growth; on the second hand, AZO exhibits poor stability when exposed to air-borne oxygen or moisture, a problem typically addressed through high-temperature post-annealing or the application of ultrathin capping films [9]. Additionally, AZO microstructural limitations, such as grain boundary scattering and reduced charge carrier mobility, remain inadequately understood.

Charge carrier mobility and free charge carriers are crucial for the electrical conductivity of TCOs, where a high charge carrier mobility increases the conductivity without compromising transparency by free-carrier absorption [6,10]. To reduce free-carrier absorption, it is crucial to decrease the concentration of free carriers and enhance the carrier mobility in the TCO, resulting in high optical transparency while preserving good electrical conductivity [11,9]. Previous studies have detailed many factors that limit the mobility of thin films, which are predominantly related to the compensation of charged defects like grain boundaries and impurities such as oxygen and aluminum [6,9,12,13]. The charge carrier mobility limitation, free carrier concentration, grain boundaries, and polycrystalline structural properties of TCO materials have been previously reported [5,12–15]. In a study conducted by A. Cruz et al., it was found that the electrical mobility (μ_e) of ITO deposited on hydrogenated nanocrystalline silicon (nc-Si: H) layers is significantly lower than that deposited on hydrogenated amorphous silicon (a-Si:H) films.

The nc-Si:H layers possessed greater crystallinity and higher surface roughness than the a-Si:H. The decrease in mobility in ITO/nc-Si:H is due to the decrease in the grain size of the ITO or an increase in trap density at the ITO grain boundaries. In contrast, AZO has nearly identical mobility when deposited on nc-Si:H and a-Si:H, which aligns with the similar structural properties observed through transmission electron microscopy using scanning nano-beam electron diffraction (NBED) [16]. Similar findings were observed in the present study. Specifically, we compared the performance of AZO by adding an ITO seed layer underneath it. In addition, Tang et al. reported that adding an ultrathin layer of ITO under AZO influences the initial grains and protects the intrinsic layer from damage, which improves the crystallinity; the grain size increases by approximately 1.1 nm to 1.7 nm [9]. Furthermore, adding the ITO layer under AZO resulted in a higher mobility and lower resistivity compared to AZO deposited directly on doped/intrinsic amorphous hydrogenated silicon. Therefore, the polycrystalline structure of both AZO and ITO, and thereby, the presence of grains and defects in the film, may affect the charge-carrier mobility [17,18]. Therefore, it is crucial to understand the microstructure of AZO thin films to enhance their electrical conductivity while preserving their transparency.

The present study aims to investigate the microstructure of AZO films using advanced electron microscopy techniques yielding insights beyond normal microstructural investigations, identify their crystalline orientation, and measure the grain size to understand how these factors influence charge carrier mobility and the electrical properties of AZO thin films with three different structures. Besides, this research examines the impact of incorporating an ITO seed layer beneath the AZO film, focusing on how this configuration enhances grain size, reduces resistivity, and improves electrical conductivity. Particular attention is given to the effects of grain size and boundaries on charge carrier mobility and the overall performance of SHJ solar cells.

The 70 nm AZO film was grown on two types of hydrogenated silicon thin films, (n/i)a-Si:H and (n)nc-Si:H/(i)a-Si:H, as well as on an approximately 10 nm ITO seed layer. Transmission electron microscopy (TEM) is an invaluable tool for examining the nano- and sub-nanoscale functional structures of materials and has been employed for studies on thin-film devices, providing deep insights and precise information by uncovering the microscopic details and correlating them with the macroscopic properties of the material [18–20]. The innovative application of four-dimensional scanning TEM (4D-STEM) with automated crystal orientation analysis was employed. The orientation and size of the grains were determined using an electron pattern-matching algorithm.

Finally, this study demonstrates an in-depth structural analysis of AZO and ITO thin films in SHJ solar cells. High resolution TEM combined with analytical TEM methods were employed to correlate the electrical properties and performance of the SHJ solar cells.

2. Experimental details

2.1. TCO deposition and solar cell fabrication

The TCO materials AZO and ITO described in this study were fabricated via magnetron sputtering, all AZO depositions were performed in a vertical in-line sputtering system by radio frequency mode (RF) of ZnO: Al_2O_3 (99:1 wt. %) planar ceramic target, with 100 sccm Argon gas flow rate, 1 kW power, 0.1 Pa pressure, and 100 °C temperature. The target area is 75 cm × 10 cm.

The ITO films were deposited in a direct current (DC) mode system from a cylindrical 99:1 wt % In_2O_3:SnO_2 target, at 5 kW power, 0.3 Pa pressure and 200 °C temperature. The diameter and length of the target is 160 mm and 690 mm, respectively. Corning EAGLE XG glass with a size of 10 × 10 cm^2 and a thickness of 1.1 mm was used as a substrate to investigate the electrical properties of the films. All the films were annealed at 170 °C for 40 min to mimic the curing step during the metallization process applied in foll SHJ structures.

Before SHJ solar cells fabrication, the wafers with size (78 × 78 mm^2) were chemically cleaned with RCA standard clean 1 (NH_4OH:H_2O: deionized water), RCA Standard Clean 2 (HCl:H_2O_2: deionized water), and dipped into 1 % HF solution for 5 min to remove the surface oxide. Subsequently, front intrinsic and n-doped hydrogenated amorphous silicon layers were deposited a-Si:H(i/n) with a thickness (4 nm/4 nm) and rear intrinsic and p-doped hydrogenated amorphous a-Si: H(i/p) (6 nm/10 nm) stack layers were deposited on the texture surfaces by plasma enhanced chemical vapor deposition (PECVD) using a AK Inline 1000 system from Meyer Burger. Next, ITO and AZO layers were deposited via sputtering, with the detailed AZO and ITO parameters described above. For SHJ solar cells with nc-Si:H, detailed parameters have been previously reported in [21]. For SHJ solar cells with ITO/AZO layers, only the carrier speed was adjusted to maintain the desired film thickness, while the remaining deposition parameters were kept the same. For the ITO seed layer, the thickness is maintained at 10 nm. The film thickness was determined by spectroscopic ellipsometry using J. A. Woollam M 2000 system. Finally, Ag fingers were screen printed on both sides and cured at 170 °C for 40 min using a Micro-tec Co. MT-650TVC screen printer with a low-temperature silver paste by Kyoto Elex.

A schematic illustration of the SHJ solar cells used in this study is shown in Fig. 1(a). A rear-junction SHJ solar cell was fabricated on an n-type Czochralski (Cz) silicon wafer. On the front side, and for simplicity, we named the samples cell 1, consisting of (n)a-Si:H, cell 2 with (n)nc-Si:H followed by AZO and cell 3, which has (n) a-Si:H, ITO, and AZO layers. Fig. 1(b) shows the zoomed-in view of the front side of Fig. 1. a. Rear-junction SHJ solar cells were produced using n-type Czochralski silicon wafers ⟨100⟩ from LONGi with a thickness of 135 μm and a resistivity of 1 Ohmcm. The film thicknesses are shown in Fig. 1(b) to fulfil the requirements of the SHJ solar cells.

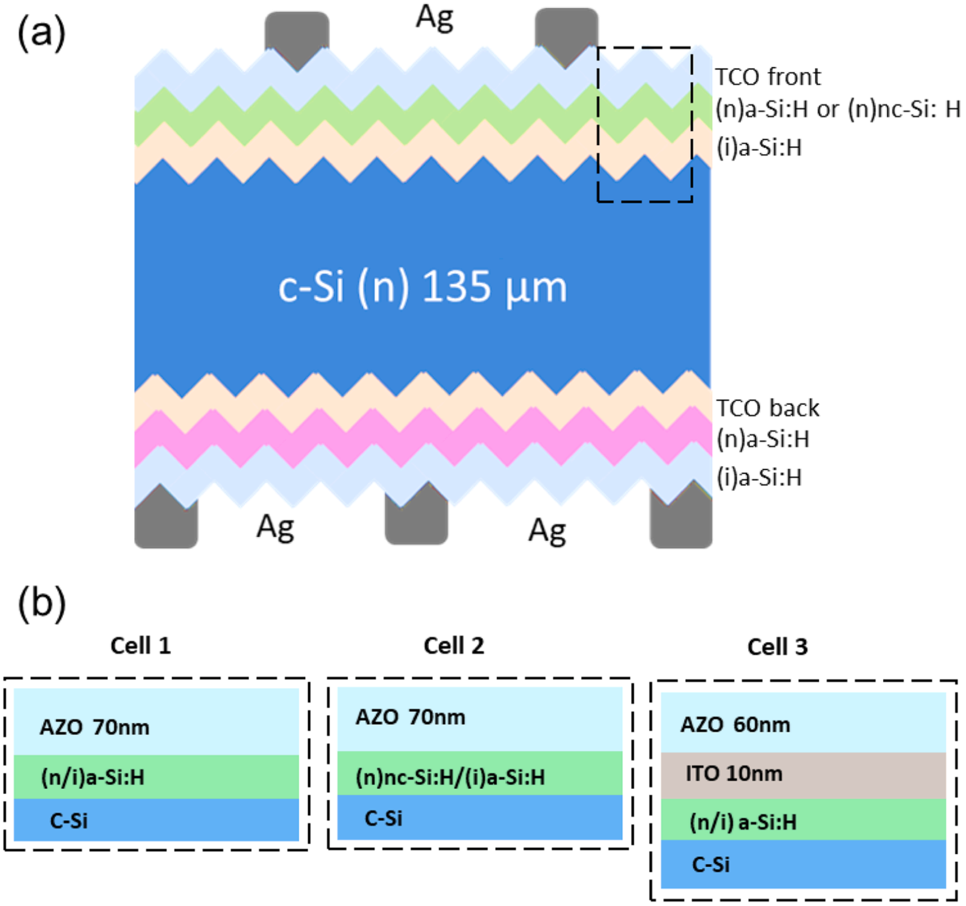

Fig. 1. (a) The schematic illustration of a standard n-type c-Si substrate SHJ solar cell, the window layers of three groups of SHJ cells fabricated for this study (b) the zoomed-in view of the front side of (a) **Cell 1**: AZO/(n/i) a-Si:H **Cell 2**: AZO/(n)nc-Si: H/(i)a-Si:H **Cell 3**: AZO/ITO/(n/i)a-Si:H.

2.2. Sample characterization

The charge carrier concentration, charge carrier mobility, and resistivity of the AZO and ITO films on glass substrates were measured using Hall measurements in the van der Pauw geometry. To evaluate the solar cell performance, the current density-voltage (*J-V*) characteristics, surface reflectance, and external quantum efficiency (*EQE*) were tested under standard conditions (25 °C, AM 1.5 G, 100 mW/cm^2) using a LOANA characterization system from pv-tools with a wave labs Sinus 220 light source.

Cross-sectional TEM specimens were prepared using the dual-beam focused ion beam (FIB) method on FEI Helios NanoLab 460F [22]. A FEI Tecnai F20 TEM operated at 200 kV was used to obtain high-resolution TEM images of the thin films on the solar cell, and the Gatan Digital Micrograph software was used for image processing. The AZO and ITO film phases were characterized using grazing incidence x-ray diffraction (GIXRD) measurements, using a Bruker D8 Advance diffractometer with Lynxe XE stripe detector operated in 0D-integration mode. The X-ray source utilized Cu Kα radiation (λ = 1.5406 Å). The diffraction patterns were recorded over a 2θ range of 15° to 75° The effective carrier lifetime of the samples with symmetrical passivation layers was measured using the quasi-steady-state photoconductance (QSSPC) technique using a Sinton Instruments WCT-120 lifetime tester [9]. Elemental composition analysis and line scans for different regions along the thin film were conducted using energy-dispersive X-ray spectroscopy (EDX) performed on a Thermo Fisher Scientific (TFS) Spectra operated at 300 kV. The STEM-EDX line scans were recorded and evaluated using the TFS Velox software. Detailed investigation of the orientation, phase, and sizes of the grains were performed by integrated and near real time 4D-STEM data acquisition and analysis using a TESCAN TENSOR operated at an acceleration voltage of 100 kV.

At each pixel in the STEM dataset, TENSOR rapidly acquired a diffraction pattern with a size of 120 mrad and a precession angle of 0.8° [23]. The template of the diffraction pattern was created using the Crystallographic Information Framework (CIF) file for each material. AZO is a hexagonal wurtzite belonging to the space group P63mc, with lattice constants of $a = 3.2495$ Å and $c = 5.2069$ Å (JCPDS #36–1451). ITO is a cubic bixbyite, and the symmetry of the space group is (Ia3 #206), with a lattice constant of $a = 10.117$ Å and $c = 10.118$ Å (JCPDS #06–0416). To quantitatively measure grain size from the TEM images, the basic ImageJ software was used, to analyze the typical grain sizes of AZO and ITO of approximately 100 grains and process the data to obtain an accurate distribution [24].

3. Results and discussion

3.1. Electrical performance of SHJ solar cells with AZO and AZO/ITO layers

Fig. 2 (a, b, c and d) shows the *J-V* measurements of the SHJ solar cells with different front contacts. When nc-Si:H was used, the open-circuit voltage (V_{oc}) of the SHJ solar cells was higher than that when a-Si:H was used, as shown in Fig. 2(a). However, Fig. 2(b) shows that the average short-circuit current densities (J_{sc}) of the cells with AZO/a-Si:H and AZO/nc-Si:H are similar, whereas the AZO/ITO contact has a 0.2–0.4 mA/cm^2 higher J_{sc}. Fig. 2(c) shows the fill factors (*FFs*) of solar cells with AZO-only layers, which are comparable regardless of whether they are grown on a-Si:H or nc-Si:H. A difference was observed when 10

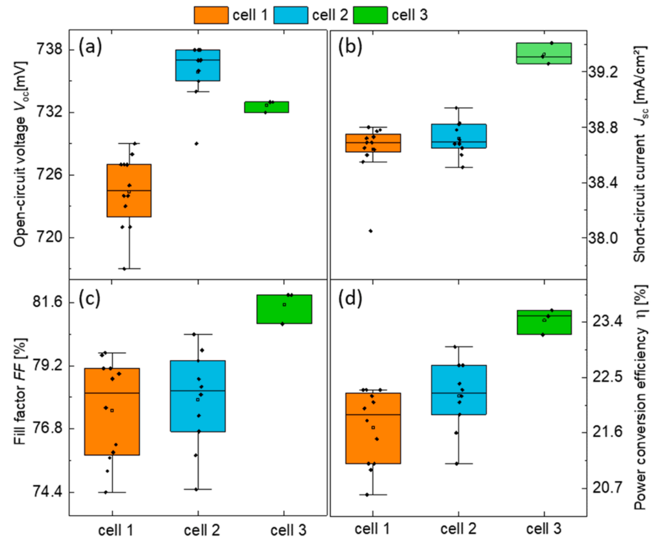

Fig. 2. (a) The open-circuit voltage (V_{oc}), (b) short-circuit current density (J_{sc}), (c) fill factor (*FF*), (d) power conversion efficiency (η) of the solar cells with AZO front contacts.

nm ITO was inserted between the AZO and n-type a-Si: H. A higher *FF* in AZO/ITO films was also reported by Tang et al., showing that the AZO/ITO stack has better contact with the a-Si:H layer and significantly improves the V_{oc} significantly to 732.7 mV compared with AZO only [9]. Overall, the power conversion efficiency (η) of AZO/ITO stacks was the highest among the cell types, reaching 23.6 % in Fig. 2(d). The different cell types originate from the AZO growth on different layers.

Fig. 3 (a and b) show the electrical properties of the AZO films. Specifically, the resistivity and carrier concentration measurements indicate that cell 1, which uses AZO only, has a resistivity of 2.01 × 10^{-3}Ohmcm. Cell 2 also has a slightly higher resistivity of 2.20 × 10^{-3} Ohmcm and in cell 3, the combination of AZO and ITO provided a lower resistivity of around 1.43 × 10^{-3} Ohmcm, this is attributed to the superior charge carrier mobility in cell 3 and can translate into a reduced series resistance, leading to a higher *FF* and improved power conversion efficiency, as shown in Fig. 2 (c and d). Ultimately, in cell 1, AZO-only films typically reveal a good charge carrier concentration in the range of 1.86 × 10^{20}cm^{-3}, whereas cell 2 reveals a higher charge carrier concentration of 2.40 × 10^{20} cm^{-3}. However, cell 3 with AZO/ITO has a charge carrier concentration of 2.16 × 10^{20} cm^{-3}. Despite cell 2 having the highest charge carrier concentration among all the cells, it had a lower charge carrier mobility, as shown in Fig. 3(b).

Nevertheless, the improvement in the charge carrier mobility of the AZO/ITO layer (up to 20.3 cm^2/Vs) might be a result of the larger grain size of 34 nm, allowing more efficient charge carrier transport compared to moving through the AZO/ITO layer more easily, reducing recombination losses, and resulting in more efficient solar cells with a higher *FF* and improved overall electrical performance, as shown in Fig. 2.

On the other hand, the charge carrier mobilities are 16.7 cm^2/Vs and 14.1 cm^2/Vs, and the grain sizes of 31 nm and 26 nm for cells 1 and 2, respectively, as shown in Fig. 3(b). The lower charge carrier mobility might be due to smaller grain sizes compared with the cell 3 AZO/ITO double-layer; for example, in the case of cell 2, the small and undefined grains, especially close to the interface of the nc-Si:H, lead to increased grain boundary scattering and subsequently increase the resistivity, as will be discussed later.

In general, the increase in charge carrier mobility is ascribed to the larger grain size, which reduces grain boundary scattering, allows for better carrier transport, and lowers the resistivity of the film. Meanwhile, from the electrical properties, cell 3 exhibited a higher charge carrier mobility and a larger *FF* than the AZO-only structure in cells 1 and 2 regardless of the charge carrier concentration, which means that

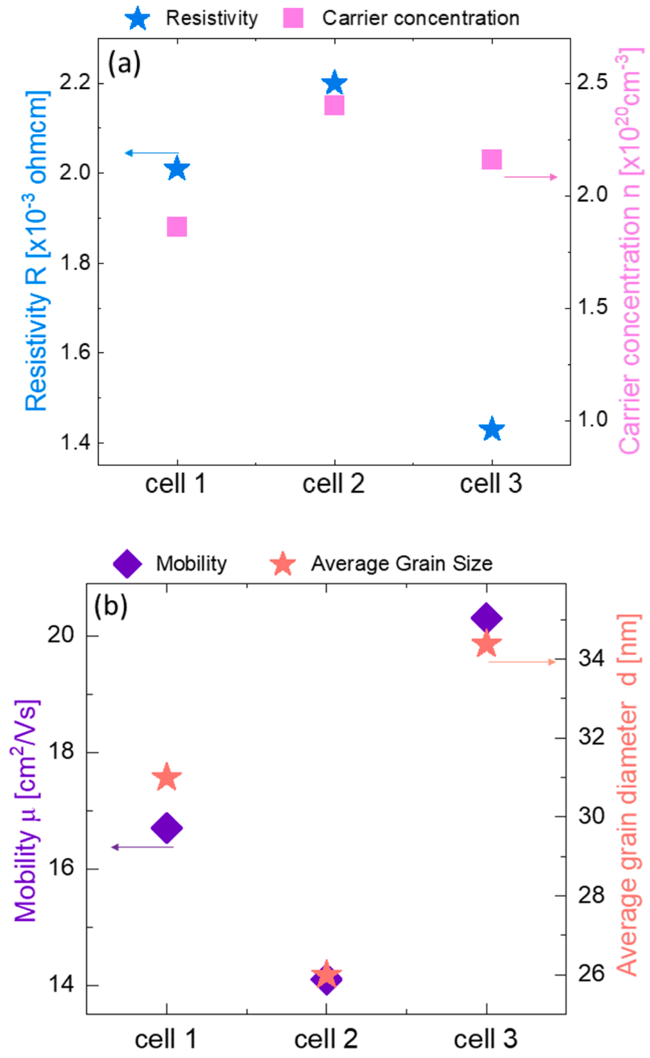

Fig. 3. (a) Resistivity and carrier concentration for the three cells in this study, and (b) Charge carrier mobility and average grain diameter.

the charge carrier concentration may not affect it as much as the charge carrier mobility [15,25]. However, Zhang et al. examined the impact of low sputtering pressure on the structural, electrical, and optical characteristics of AZO thin films. The study was conducted on the effects of reduced working pressure on AZO thin films at ambient temperature using RF magnetron sputtering, regardless of the Ar flow rate. As the working pressure varied from 0.02–0.32 Pa, changes in morphological properties were observed. The lowest resistivity achieved is 6.40 × 10^{-4} Ohmcm, with charge carrier mobility playing a more significant role than carrier concentration in this outcome [15].

In order to link the electrical and optical properties with the grain size and orientation detailed descriptions of the following literatures, Park et al. showed that the grain size was calculated in the range of 46 nm. The lowest electrical resistivity was 4.65 × 10^{-4} to 2.98 × 10^{-4} Ohmcm and the average transmittance was 79 to 82 % [26]. Zhang et al. estimated the grain size of AZO deposited by magnetron sputtering to be in the range of 36.3 nm. The grain sizes of the different samples were calculated from the corresponding full width at half maximum (FWHM) of the (0002) diffraction reflection based on the Scherrer formula, with an electrical resistivity of 6.4 × 10^{-4} Ohmcm and the average transmittance of 74 % [15]. In addition, the grain size ranged from 30 nm to 39 nm. Misra et al. reported the electrical resistivity was 1.90 × 10^{-2} to 8 × 10^{-4} Ohmcm and the average transmittance was above 87 % [27]. Interestingly, all these studies showed a considerable influence of grain size on the electrical properties of AZO films, one can find further information on the optical properties of the SHJ solar cells with AZO thin layers reported in Ref [21,28,29]. AZO and ITO as front layers in SHJ solar cells require high transparency across the UV–Vis-NIR wavelengths. In our laboratory, we have successfully developed AZO and ITO films with transparency exceeding 80 %, making them well-suited for our applications. Regarding the AZO/ITO bilayer, we have ensured that our films maintain sufficient transmittance and low absorptance, which are crucial for allowing light to reach the absorber layer in SHJ solar cells. Additionally, we carefully control the thickness of the bilayer AZO/ITO to function as an effective anti-reflection coating, thereby enhancing the generation of photogenerated carriers. Furthermore, the improved crystallinity of the bilayer ITO/AZO film enhances charge carrier mobility, leading to lower film resistivity and better electrical performance.

A comprehensive review of the literature, as presented in Table 1, highlights the performance of AZO-related SHJ solar cells. Our AZO-based SHJ solar cell stands out with remarkable efficiency.

3.2. *Structural evaluation*

Fig. 4. shows the HRTEM images for cell 1 and the corresponding Fast Fourier transform (FFT), providing detailed structural insights into the typical columnar grains of AZO thin films deposited by RF sputtering on the a-Si:H film. Fig. 4(a) shows HRTEM images of one grain of the AZO film with a size of 53.8 nm and Fig. 4(b) shows a different grain of the same layer with a size of 26.2 nm. A similar experiment was conducted in cell 2, composed of AZO on nc-Si:H, resulting in even smaller grain sizes. However, one can see it in the Appendix Section Fig. A1. The FFT diffraction pattern exhibited a strong intensity corresponding to an interplanar spacing of $d = 0.2610$ nm for the (0002) plane of the AZO hexagonal phase. The preferential growth along the c-axis, perpendicular to the silicon substrate, as indicated by the arrow in the growth direction is a characteristic feature of highly oriented ZnO-based thin films. This vertical grain alignment can reduce grain boundary density along the conduction path, minimizing carrier scattering and charge trapping at defect sites, which can significantly impact electron transport and reduce series resistance in solar cells. The combination of HRTEM imaging and FFT analysis confirmed the crystalline nature of the AZO grains. The strong alignment along the (0002) plane supports the idea that the deposition process creates a film with a well-defined crystalline structure, which generally improves the conductivity of the AZO thin film [15], electron mobility, resistivity, and overall performance of the AZO layer.

Figs. 5(a) and (b) show the HAADF-STEM and EDX elemental maps of the sample with the thin film in cell 3 consisting of the ITO/AZO double-layer. Fig. 5(c) show the elemental maps of silicon (yellow), indium (blue), zinc (green), and oxygen (red). Indium (In) is the brightest line in the HAADF-STEM image owing to its large atomic number based on Z-contrast imaging. Therefore, the darker contrast indicates a light element and the bright contrast indicates a heavier element at that location [35], which offers an understanding of the elemental distribution within the AZO/ITO double-layer.

Table 1
Summary of the performance of AZO-related SHJ solar cells, adapted by [9].

AZO Percentage (%)	V_{oc} (mV)	J_{sc} (mA/cm^2)	*FF* (%)	η (%)	Ref. (Year)
100	708	34.35	79.1	19.2	[7] (2015)
100	718	37.0	76.1	20.2	[30] (2018)
100	730	39.6	78.9	22.8	[31] 2018)
50	/	/	/	22.6	[32] (2019)
100	/	/	/	22.5	[32] (2019)
/	726	40.81	80.87	23.96	[33] (2019)
50	741	39.0	81.6	23.6	[34] (2021)
85.6	**738**	**38.62**	**83.4**	**23.8**	**[9] (2023)**

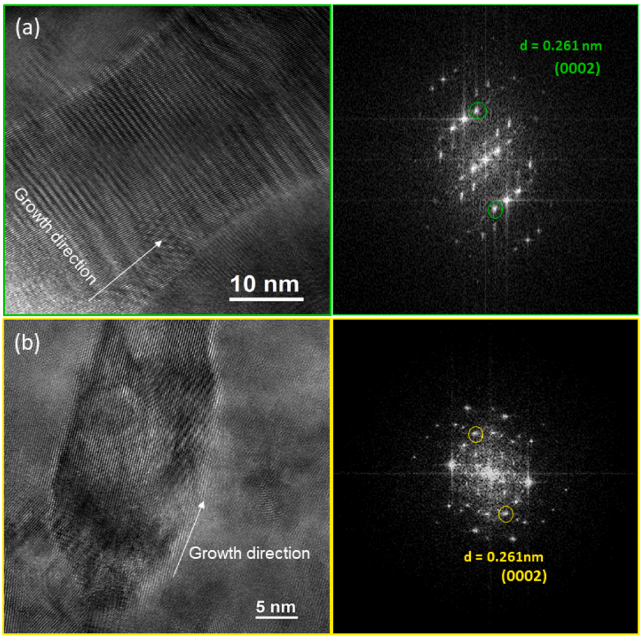

Fig. 4. (a) HRTEM image of sample cell 1 with a scale bar of 10 nm has an average grain size of 53.8 nm and the corresponding FFT pattern; (b) HRTEM image of sample cell 1 with a scale bar of 5 nm and its average grain size of 26.2 nm and the corresponding FFT pattern.

Further observations of the columnar microstructures of ZnO-based thin films have been reported in Refs. [18,31]. The microstructure and morphology of ZnO-based materials were studied using x-ray diffraction (XRD) characterization as described in Refs [17,14,36–38]. For cell 1 with the AZO-only film, x-ray diffraction showed stronger reflections for the (0002) and (1013) planes, indicative of the polycrystalline wurtzite hexagonal structure. In contrast, cell 3 with the ITO/AZO film exhibited (222), (0002), and (1013) reflections. In the XRD pattern, the (0002) and (1013) reflections emerge from the AZO film and the cubic (222) reflection from ITO appears, indicating that the ITO crystallites were preferentially arranged with the (222) planes parallel to the substrate surface, which can contribute to improved electrical conductivity and charge carrier mobility [9], as shown in Fig. 5(d). The observed changes in crystallographic structure between AZO-only and ITO/AZO films further emphasize the role of the ITO seed layer in enhancing grain growth and thus reducing resistive losses in SHJ solar cells.

3.3. *Orientation mapping and influence of grain size and boundaries*

Analytical investigation via 4D-STEM mapping allows the selection of orientation/phase measurements for near-real-time orientation and phase mapping of single- and multiphase polycrystalline and amorphous materials. In this method, an electron beam with approximately 1 nm in size was scanned across the specimen while acquiring diffraction patterns at a high speed of hundreds of frames per second using an integrated hybrid-pixel direct electron detector. A template-matching algorithm is used to index each experimental diffraction pattern by automatically matching the templates from the kinematic diffraction modelling. The diffraction templates were precomputed for each orientation of the given material, based on its crystal structure [23]. Template matching is fully automated and can generate an estimate of the measurement confidence using cross-correlation between the templates and experimental diffraction patterns. Precession electron diffraction was also applied to average out dynamical diffraction effects and increase the reliability of orientation and phase identification. A reliability map is particularly useful for identifying grain boundaries because these areas typically have low reliability [39].

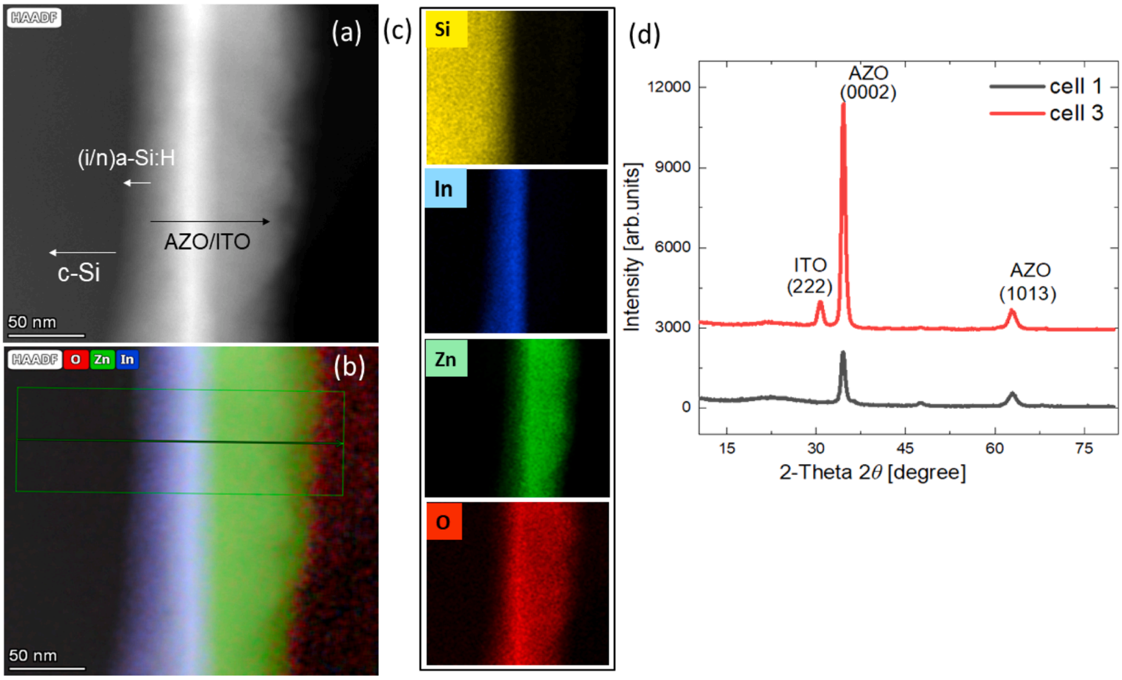

Fig. 5. (a)High annular dark-field (HAADF) STEM image obtained at a comparable position within cell 3, (b) The composite image of elemental mapping (indicated with the arrow the same with growth direction), (c) The compositional mapping for each element is silicon (yellow), indium (blue), zinc (green), and oxygen (red), (d) XRD pattern of the TCO film, where red indicates cell 3 and black indicates cell 1, adapted from [9].

Fig. 6 shows the BF-STEM images recorded along the [100] direction of the silicon substrate; the scanning area for each image was 2 μm × 2 μm, providing a resolution of approximately 2 nm per spot size. Fig. 6 (a, b, and c) show the virtual BF-STEM images and the diffraction patterns for the silicon substrate. The formation of sharp edges of the textured film was observed in all three samples, indicating a good growth quality and characterization tool resolution. Fig. 6(a) shows the AZO film deposited on the (n/i) a-Si:H in cell 1, a predominantly perpendicular grain orientation relative to the silicon substrate, forming a columnar structure. This columnar growth is typical for RF sputtered AZO films and is associated with improved carrier transport due to reduced grain boundary scattering [14]. However, the grain size remains relatively moderate, which can still lead to some resistive losses in the AZO layer, especially close to the interface with the silicon substrate. Fig. 6(b) displays the AZO film deposited on the nc-Si:H in cell 2, which still has perpendicular growth with respect to the substrate similar to cell 1; however, we noticed small grains close to the substrate. These smaller grains can introduce a higher grain boundary density, increasing charge carrier scattering and limiting charge carrier mobility. This observation suggests that the underlying nc-Si:H layer may influence the nucleation process, leading to a finer grain structure near the interface. Fig. 6(c) shows the AZO with the ITO seed layer in cell 3, the grains are larger than those of cells 1 and 2. The presence of the ITO seed layer appears to promote enhanced grain growth and improved crystallinity, resulting in reduced grain boundary density and higher charge carrier mobility. The larger grain structure in cell 3 correlates well with the improved electrical conductivity and reduced resistivity observed in previous measurements. While Fig. 6 provides BF-STEM images for the structural evolution of the AZO and AZO/ITO films, the subsequent Fig. 7 further clarifies the grain size distribution and structural characteristics.

Fig. 7 (a, b, and c) show the phase reliability maps for the first column (a) cell 1 with AZO deposited on a-Si:H, the second column (b) cell 2 with AZO deposited on nc-Si:H, and the third column (c) cell 3 with AZO deposited on the seed layer ITO. The orientation phase maps display only two different phases in all cells, confirming the expected materials composition and phase distribution across the films, which are

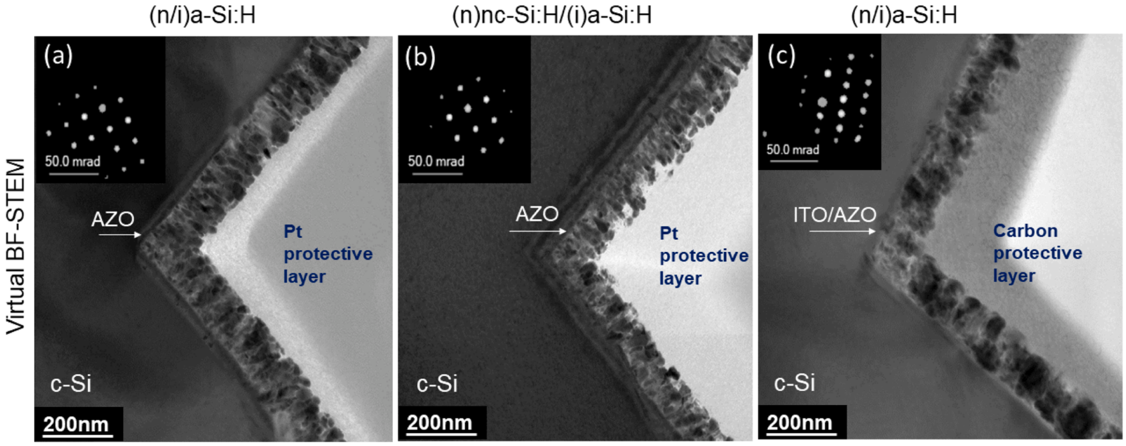

Fig. 6. (a) shows the virtual BF-STEM and diffraction patterns of the silicon substrate in the inlets.

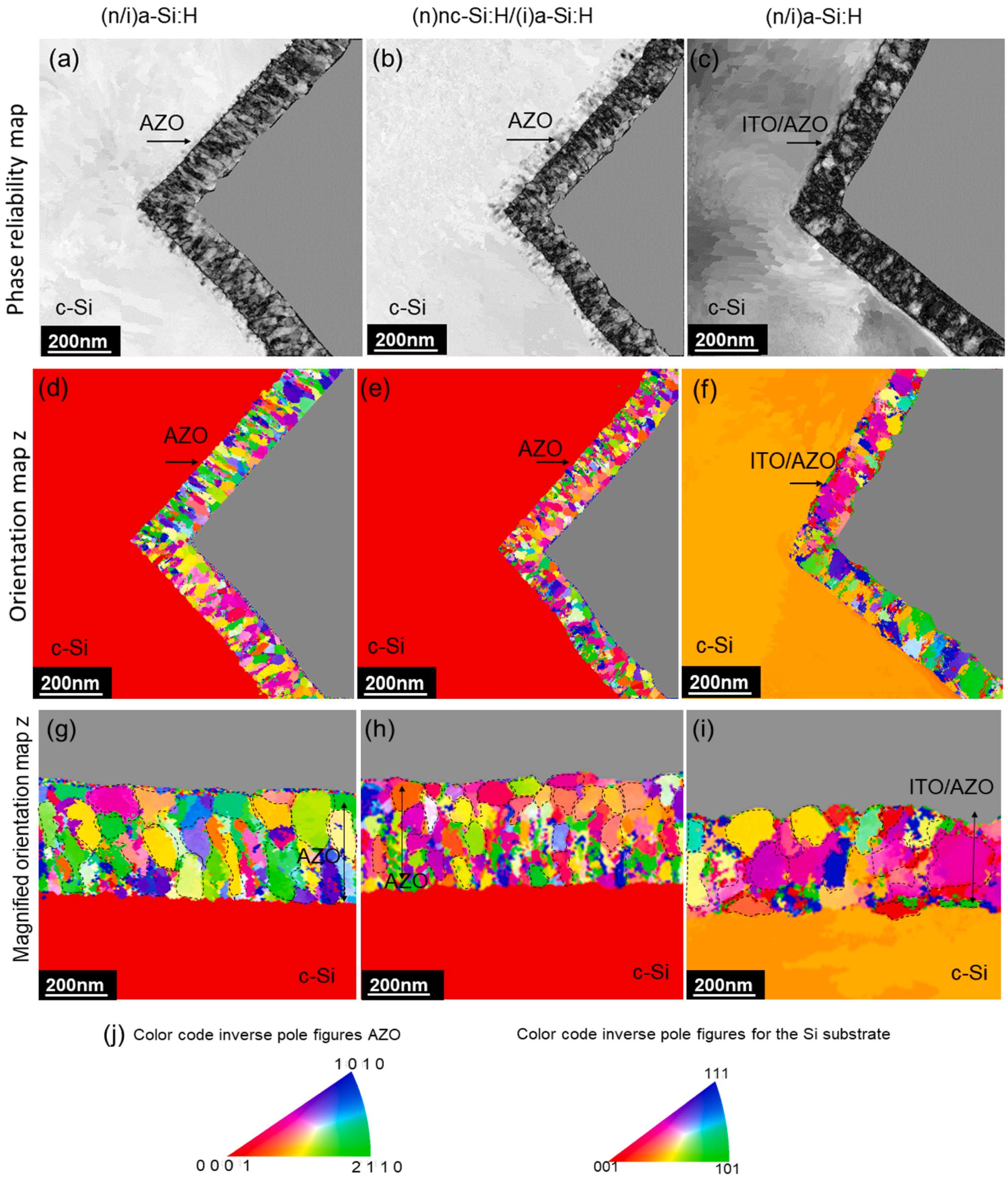

Fig. 7. (a, b and c) shows the phase reliability map, for cells 1, 2, and 3 from left to right. (d, e, and f) show the orientation map along the electron beam direction (z-axis) of cells 1,2 and 3 from left to right. (g, h, and i) show a magnified view of the respective orientation mapping along the z-axis the gray color for the protective layer, and (j) color code inverse pole figures for the Si substrate and AZO.

Si and AZO.

Fig. 7 (d, e, and f) shows the orientation map along the z-direction, where the electron beam of the microscope is along the z-direction of the grains, in which the grains in the AZO films for all cells tend to overlap and expand along the film thickness in the textured samples, resulting in depth-related uncertainties in the orientation maps. The texturing effect is particularly relevant for understanding charge transport behavior, as grain overlap and alignment along the growth direction can influence charge carrier mobility and resistivity. Fig. 7(d) shows the orientation map for cell 1, where AZO deposited on the a-Si:H layer shows somewhat large and laterally extended grains along the Silicon substrate, and the images also show the existence of different crystalline phases. Fig. 7 (e) for AZO deposited on nc-Si:H in cell 2 shows undefined and disordered small grains in the middle of the film, gradually forming randomly on the film surface. Leading to a more heterogeneous and less organized structure compared to cell 1. This irregular grain distribution may contribute to higher resistivity due to increased grain boundary scattering, which can impede charge carrier mobility and negatively affect the electrical performance of the AZO layer.

Fig. 7(f) shows the AZO sample on the ITO seed layer in cell 3, which exhibits undefined and irregular large grains along the Silicon substrate. which contrasts with the more uniform columnar grains seen in cells 1 and 2. The structural differences observed in cell 3 suggest that the ITO seed layer plays a critical role in modifying grain growth dynamics, promoting lateral grain expansion near the substrate and facilitating a more efficient charge transport pathway.

These are evident in the orientation maps and are clearly visible in Fig. 7 (g, h, and i), which show the magnified areas of the orientation maps in Figures (d, e, and f), respectively. For simplicity, we masked the protective layer with grey color in Fig. 7. The color-coded inverse pole figures for the silicon substrate on the right and the AZO on the left are shown in Fig. 7(j), considering that the color-coded orientation maps from the Silicon substrate, which is the cubic phase, are different from those of AZO thin films, which is hexagonal.

In summary, Figs. 6 and 7 demonstrate a structural comparison of the three different cell configurations: cell 1: AZO on a-Si:H, cell 2: AZO on nc-Si:H, and cell 3: AZO/ITO. The 4D-STEM complemented by an automated crystal orientation analysis is also supported by the TEM images in Figure A 2. The orientation and size of the grains were determined for all three cell types. Cell 1 had larger grains that were typically started at the interface. However, sample cell 2 started with small grains close to the substrate and the grain size increased along the thickness of the AZO film, which may explain the higher resistivity of cell 2. Typically, most of the grains in cells 1 and 2 were perpendicular to the substrate. This can be attributed to the on-par fill factor for cells 1 and 2. Sample cell 3 demonstrated higher grain sizes in the lateral direction close to the substrate and exhibited some perpendicular growth at the top of the AZO film, which was attributed to the lower resistivity of cell 3 and a higher fill factor FF. On the other hand, cell 3 demonstrated superior grain growth, with larger lateral grains near the substrate and a transition to perpendicular growth at the top of the AZO film. This unique microstructure is likely responsible for lower resistivity and an improved *FF* in cell 3, further confirming the beneficial effects of incorporating an ITO seed layer in optimizing AZO-based TCO performance for SHJ solar cells.

Fig. 8 shows the quantitative evolution of the change in the microstructure, specifically the grain size and diameter distributions, for different cell types. A minimum of 100 grains was selected, and the histograms for the grain diameter were measured based on the orientation of the grain boundary annotation layer.

The identified size of the grains varies from 5–90 nm for all cells, where smaller grains were observed in sample cell 2, whereas larger grains were observed in sample cell 3. Suggesting a direct influence of the underlying substrate and seed layer on grain growth dynamics.

For sample cell 1, as shown in Fig. 8(a) with AZO deposited on a-Si:H, grain boundaries were present in columnar growth, originating from the initial stages of growth. Fig. 8(b) shows sample cell 2 with AZO deposited on nc-Si:H, which exhibited irregular and small grains during the initial stages of the films. Fig. 8(c) sample cell 3 with AZO and seed-layer ITO exhibited large grains and irregular boundaries. The ITO seed layer appears to promote enhanced grain growth, facilitating the formation of fewer grain boundaries and a more uniform crystalline structure. The increase in grain size in cell 3 correlates well with its lower resistivity and higher charge carrier mobility, as observed in previous electrical performance. The irregular grain boundaries, while present, are significantly less dense than those in cell 2, further supporting the role of ITO in improving grain connectivity and overall film quality.

The statistical study revealed that the AZO deposited on a-Si: H had an average grain size of 31 nm, the AZO deposited on nc-Si:H has an average grain size of 26 nm and the AZO deposited on seed layer ITO had a 34 nm as illustrated in Fig. 8 (d, e, and f).

The correlation between grain size, film morphology, and electrical conductivity suggests that optimizing the underlying layer composition can be an effective strategy for improving charge transport efficiency and device performance.

Fig. 9 (a and b) shows a schematic representation of the grain sizes

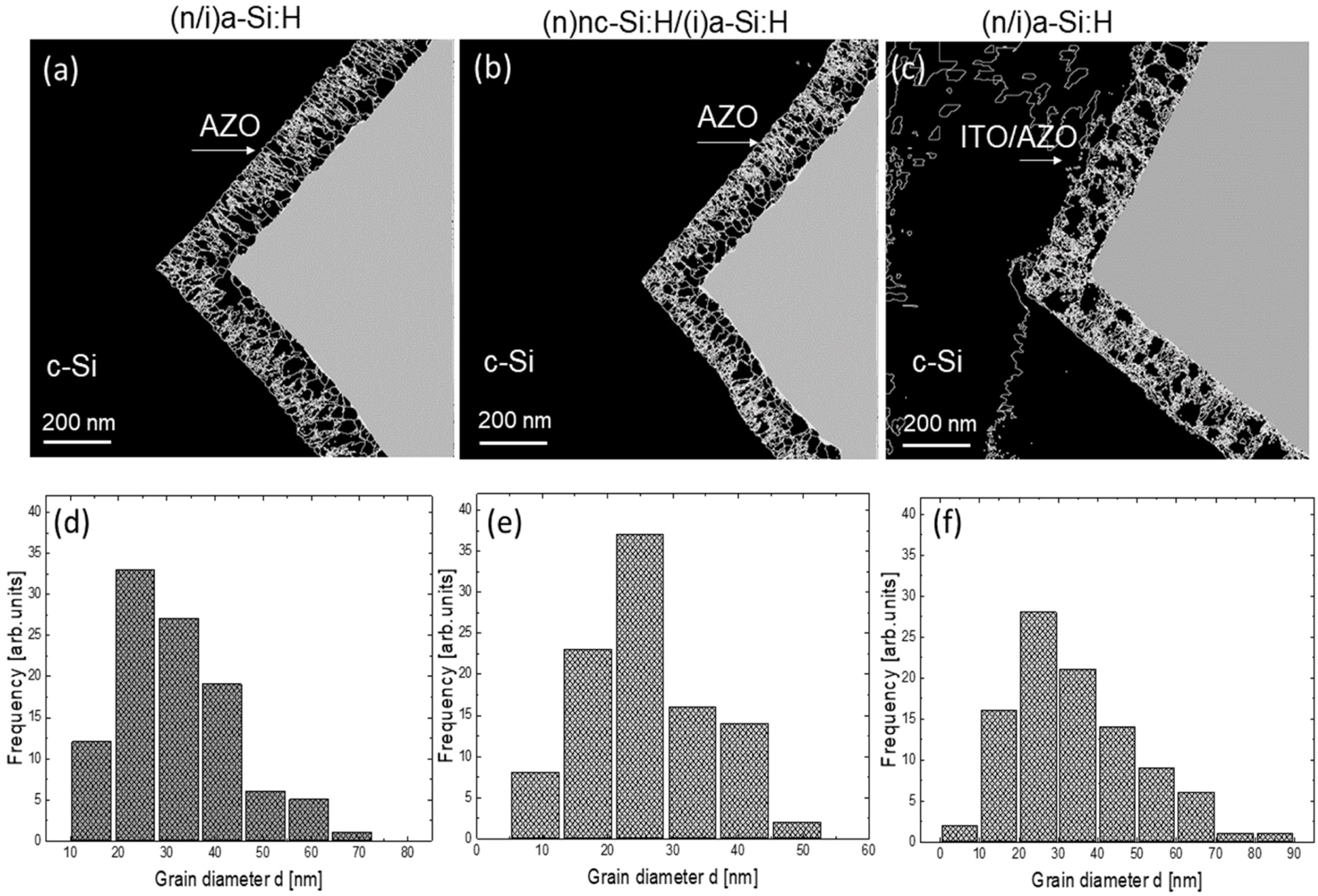

Fig. 8. (a, b, and c) Grain boundary annotation layer for cell 1 with AZO/a-Si: H, cell2 with AZO/nc-Si:H, and cell3 with AZO/ITO, respectively; (d, e, and f) Statistical analysis of grain size distribution.

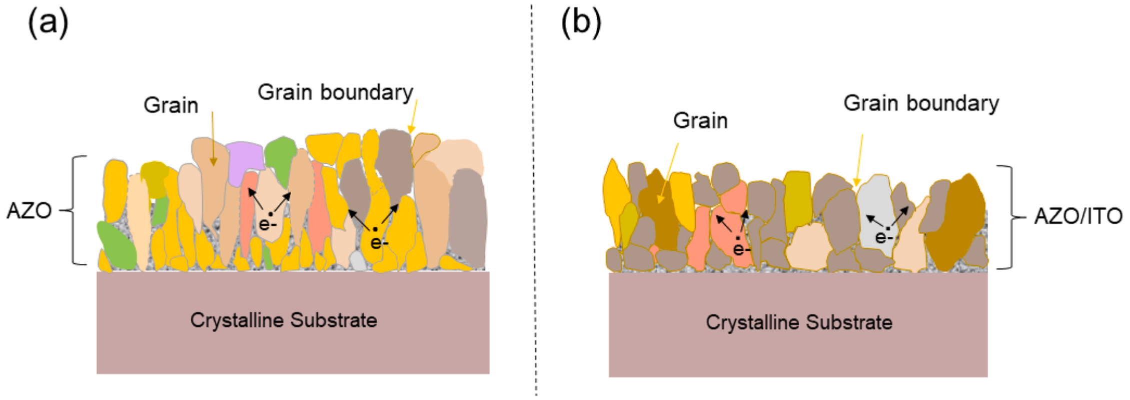

Fig. 9. (a and b) Schematic illustration of the grain sizes and boundaries of the basic SHJ AZO deposited on (n/i) a-Si:H and AZO deposited on hydrogenated amorphous silicon with an ITO layer underneath, respectively.

and boundaries based on STEM images. The orientation analysis of the two structures shows the crystal structure of cell 1: AZO deposited on (n/i)a-Si:H/c-Si, and for cell 3: AZO with an ITO seed layer underneath and (n/i)a-Si:H/c-Si, respectively. Structural defects, such as grain boundaries, vacancies, and impurities, cause scattering during charge carrier movement, reducing charge carrier mobility. In the case of AZO, the columnar grains are oriented perpendicular to the substrate owing to the natural growth of ZnO, which possesses a polar lattice that exhibits piezoelectricity along the c-axis [40]. In contrast, the nonpolar nature of In_2O_3 means that its surfaces do not exhibit spontaneous polarization effects similar to those of ZnO [25,41]. This might also explain why the growth behavior of ITO contributes to high lateral conductivity, which is further supported by the increased carrier concentration and high fill factor, featuring a double-layer AZO/ITO in cell 3.

Overall, the improved mobility and higher fill factor observed for the AZO/ITO sample cell 3 can be largely attributed to its large grain size and grain boundaries. Conversely, the reduced charge carrier mobility of AZO on nc-Si:H can be attributed to a decrease in grain size within the bulk material. This may also suggest an increase in the film resistivity and a decrease in the fill factor for cell 2. Interestingly, the AZO on a-Si:H exhibited a consistent range of charge carrier mobility and fill factor, similar to that of AZO on nc-Si:H. This suggests that grain size alone may not be the sole determinant of electrical performance, and additional factors such as interface quality, defect density, and film passivation may also contribute to the overall device behavior.

4. Conclusion

In conclusion, this study presents a novel approach to investigate the microstructural of AZO transparent conducting oxide layers on silicon heterojunction solar cells using the 4D-STEM technique, thereby offering valuable insights into the microstructure and growth behavior of AZO thin films. These insights contribute to understanding the additional impact of the ITO underlying layer on the microstructure of the AZO. The technique of mapping the orientation and grain size by 4D-STEM enabled the identification of the microstructure of the AZO film. This is due to the polycrystalline structure and the small grain size of the film. This study presents a detailed structural characterization of AZO and ITO thin films on silicon heterojunction solar cells using HRTEM imaging along with analytical TEM techniques, which helped examine and analyze the grain size and orientation of the AZO films.

Analysis of the STEM images revealed some features of the AZO film grown on both the a-Si:H and nc-Si:H layers and the ITO seed layer. The first structure of AZO on a-Si:H shows columnar grains in the direction perpendicular to the substrate, which is evident in the orientation maps that are likely to enhance the carrier mobility, while the AZO film on nc-Si:H shows small grains in the center of the films that were irregularly formed on the surface, displaying irregular grain boundaries in the initial stages of the films, matching the reduced mobility. Furthermore, the structure with the ITO seed layer exhibited increased grain size and irregular boundaries. This study demonstrates the impact of the AZO and ITO seed layer film deposition processes on the grain size, structure, and electrical properties of the film.

CRediT authorship contribution statement

Sara Alkhereibi: Writing – original draft, Investigation, Data curation, Conceptualization. **Muhammad Ainul Yaqin:** Writing – review & editing. **Alexander Eberst:** Writing – review & editing. **Binbin Xu:** Writing – review & editing. **Janghyun Jo:** Writing – review & editing, Investigation. **Husain Alsamamra:** Writing – review & editing. **Andreas Lambertz:** Writing – review & editing. **Uwe Rau:** Writing – review & editing, Supervision, Resources. **Kaining Ding:** Writing – review & editing, Supervision, Resources. **Joachim Mayer:** Writing – review & editing, Supervision, Resources.

Declaration of competing interest

The authors declare the following financial interests/personal relationships which may be considered as potential competing interests: Sara Alkhereibi reports financial support was provided by Palestinian German science bridge (PGSB). Binbin Xu reports financial support was provided by CSC. If there are other authors, they declare that they have no known competing financial interests or personal relationships that could have appeared to influence the work reported in this paper.

Acknowledgement

This work was supported by the Federal Ministry of Education and Research of Germany in the framework of the Palestinian-German Science Bridge (BMBF grant number D.B.XC1436) and the Federal Ministry of Economic Affairs and Energy in the framework of the TOP project under the grant number 03EE1080B and the Helmholtz Energy Materials Foundry (HEMF) infrastructure funded by the HGF (Helmholtz association).

Appendix Section

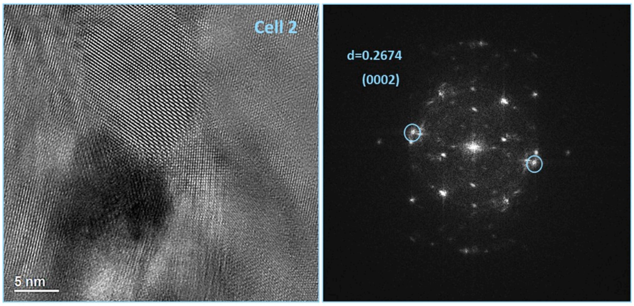

Fig. A1. HRTEM images of the structure with AZO deposited on (n)nc-Si:H/(i)a-Si:H/c-Si, with scale bars of 25 nm average grain size of 14.8 nm and the corresponding FFT pattern.

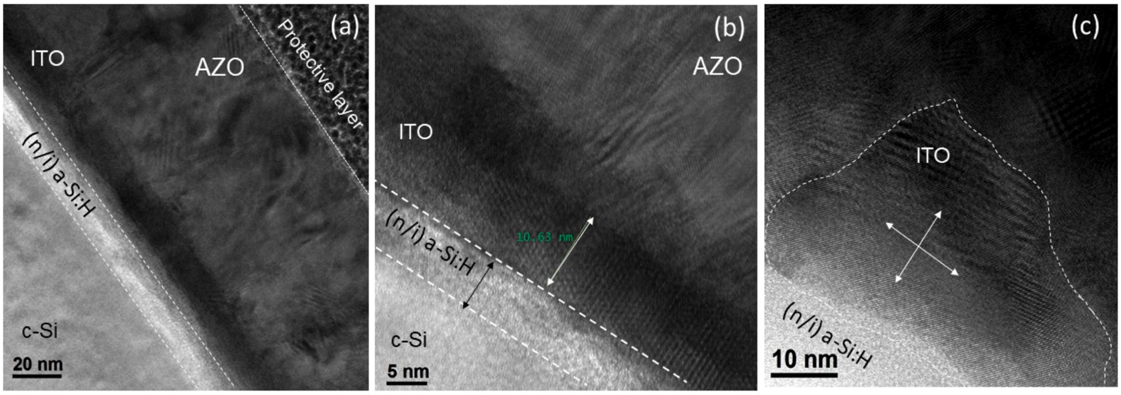

Fig. A2. HRTEM images of the structure with AZO/ITO deposited on (i/n)a-Si:H/c-Si, with scale bars of 20, 5, and 10 nm, respectively, from left to right.

(Fig. A1,Fig. A2)

Data availability

The data that has been used is confidential.

References

[1] International Technology Roadmap For photovoltaics:2024 Results, ITRPV, 2024.

[2] H. Lin, M. Yang, X. Ru, G. Wang, S. Yin, F. Peng, C. Hong, M. Qu, J. Lu, L. Fang, C. Han, P. Procel, O. Isabella, P. Gao, Z. Li, X. Xu, Silicon heterojunction solar cells with up to 26.81% efficiency achieved by electrically optimized nanocrystalline-silicon hole contact layers, Nat. Energy 8 (8) (2023) 789–799, https://doi.org/10.1038/s41560-023-01255-2.

[3] K. Yoshikawa, H. Kawasaki, W. Yoshida, T. Irie, K. Konishi, K. Nakano, T. Uto, D. Adachi, M. Kanematsu, H. Uzu, K. Yamamoto, Silicon heterojunction solar cell with interdigitated back contacts for a photoconversion efficiency over 26%, Nat. Energy 2 (5) (2017) 1–8, https://doi.org/10.1038/nenergy.2017.32.

[4] H. Sai, T. Matsui, Toward TCO-free silicon heterojunction solar cells: effect of TCO layers in electrical transport and stability, Sol. RRL. 7 (18) (2023) 2300290, https://doi.org/10.1002/solr.202300290.

[5] K. Ellmer, Past achievements and future challenges in the development of optically transparent electrodes, Nat. Photonics. 6 (12) (2012) 809–817, https://doi.org/10.1038/nphoton.2012.282.

[6] W. Huang, J. Shi, Y. Liu, F. Meng, Z. Liu, Effect of crystalline structure on optical and electrical properties of IWOH films fabricated by low-damage reactive plasma deposition at room temperature, J. Alloys. Compd. 843 (2020) 155151, https://doi.org/10.1016/j.jallcom.2020.155151.

[7] O.M. Ghahfarokhi, K. Chakanga, S. Geissendoerfer, O. Sergeev, C. Agert, DC-sputtered ZnO:Al as transparent conductive oxide for silicon heterojunction solar cells with μc-Si:H emitter, Prog. Photovolt. 23 (10) (2015) 1340–1352, https://doi.org/10.1002/pip.2570.

[8] G. Dong, J. Li, Y. Zhao, X. Ran, W. Peng, D. He, C. Jin, Q. Wang, H. Jiang, Y. Zhang, X. Cao, C. Yu, Highly efficient silicon heterojunction solar cells with ZnO:al transparent electrode and transition metal doped indium oxide interfacial layer, Prog. Photovolt. 31 (9) (2023) 931–938, https://doi.org/10.1002/pip.3697.

[9] Tang, Q. and Duan, W. and Lambertz, A. and Bittkau, K. and Yaqin, M.A. and Zhao, Y. and zhang, K. and Yang, Q. and Qiu, D. and Rau, U. and Ding, K., >85% Indium Reduction for High-Efficiency Silicon Heterojunction Solar Cells with Aluminum-Doped Zinc Oxide Contacts. Available at SSRN: https://ssrn.com/abstract=4176859 or https://doi.org/10.2139/ssrn.4176859.

[10] C. Agashe, O. Kluth, J. Hüpkes, U. Zastrow, B. Rech, M. Wuttig, Efforts to improve carrier mobility in radio frequency sputtered aluminum doped zinc oxide films, J. Appl. Phys. 95 (4) (2004) 1911–1917, https://doi.org/10.1063/1.1641524.

[11] H. Scherg-Kurmes, S. Seeger, S. Körner, B. Rech, R. Schlatmann, B. Szyszka, Optimization of the post-deposition annealing process of high-mobility In2O3:H for photovoltaic applications, Thin Solid Films 599 (2016) 78–83, https://doi.org/10.1016/j.tsf.2015.12.054.

[12] A. Valla, P. Carroy, F. Ozanne, D. Muñoz, Understanding the role of mobility of ITO films for silicon heterojunction solar cell applications, Solar Energy Materials and Solar Cells 157 (2016) 874–880, https://doi.org/10.1016/j.solmat.2016.08.002.

[13] K. Ellmer, R. Mientus, Carrier transport in polycrystalline ITO and ZnO:Al II: the influence of grain barriers and boundaries, Thin Solid Films 516 (17) (2008) 5829–5835, https://doi.org/10.1016/j.tsf.2007.10.082.

[14] P. Šotová, P. Novák, T. Kozák;, Characterization of columnar structure of sputtered AZO films by electron microscopy for grain boundary scattering model, AIP. Conf. Proc. 2411 (1) (2021) 030007, https://doi.org/10.1063/5.0070522, 2 November.

[15] Z. Zhang, Y. Tang, J. Chen, J. Chen, Influence of low sputtering pressure on structural, electrical and optical properties of Al-doped zinc oxide thin films, Physica B 495 (2016) 76–81, https://doi.org/10.1016/j.physb.2016.05.015.

[16] A. Cruz, R. Schlatmann, B. Stannowski, F. Ruske, A. Eljarrat, P.P. Michałowski, A. B. Morales-Vilches, S. Neubert, E. Wang, C.T. Koch, B. Szyszka, Influence of silicon layers on the growth of ITO and AZO in silicon heterojunction solar cells, IEEe J. Photovolt. 10 (2020) 703–709, https://doi.org/10.1109/JPHOTOV.2019.2957665.

[17] N.P. Patel, K.V. Chauhan, Structural, optical and electrical study of ZnO:Al thin films: a review, Mater. Today 62 (2021) 3386–3396, https://doi.org/10.1016/j.matpr.2022.04.268.

[18] G. Kiriakidis, M. Suchea, S. Christoulakis, P. Horvath, T. Kitsopoulos, J. Stoemenos, Structural characterization of ZnO thin films deposited by dc magnetron sputtering, Thin Solid Films 515 (24) (2007) 8577–8581, https://doi.org/10.1016/j.tsf.2007.03.111.

[19] B. Mendis, K. Durose, Prospects for electron microscopy characterisation of solar cells: opportunities and challenges, Ultramicroscopy 119 (2012) 82–96, https://doi.org/10.1016/j.ultramic.2011.09.010.

[20] Abou-Ras, D., Nichterwitz, M., Romero, M.J., .& Schmidt, S.S. (.2016). Electron Microscopy on Thin Films for Solar Cells. 371–420. https://doi.org/10.1002/9783527699025.ch14.

[21] D. Qiu, W. Duan, A. Lambertz, A. Eberst, K. Bittkau, U. Rau, K. Ding, Transparent conductive oxide sputtering damage on contact passivation in silicon heterojunction solar cells with hydrogenated nanocrystalline silicon, Sol. RRL. 6 (10) (2022) 2200651, https://doi.org/10.1002/solr.202200651.

[22] J. Mayer, L.A. Giannuzzi, T. Kamino, J. Michael, TEM sample preparation and FIB-induced damage, MRS Bull. 32 (5) (2007) 400–407, https://doi.org/10.1557/mrs2007.63.

[23] D. Van Der Wall, Scanning transmission electron microscopy done right, Micros. Today 31 (2) (2023) 15–17, https://doi.org/10.1093/mictod/qaad009.

[24] S. Zhang, C. Wang, Precise analysis of nanoparticle size distribution in TEM image, Methods Protoc. 6 (4) (2023) 63, https://doi.org/10.3390/mps6040063.

[25] K. Wang, P. Jiao, Y. Cheng, H. Xu, G. Zhu, Y. Zhao, K. Jiang, X. Zhang, Y. Su, ITO films with different preferred orientations prepared by DC magnetron sputtering, Opt Mater 134 (2022) 113040, https://doi.org/10.1016/j.optmat.2022.113040.

[26] H. Park, S. Qamar Hussain, S. Velumani, A.H. Tuan Le, S. Ahn, S. Kim, J. Yi, Influence of working pressure on the structural, optical and electrical properties of sputter deposited AZO thin films, Mater. Sci. Semicond. Process. 37 (2015) 29–36, https://doi.org/10.1016/j.mssp.2014.12.076.

[27] P. Misra, V. Ganeshan, N. Agrawal, Low temperature deposition of highly transparent and conducting Al-doped ZnO films by RF magnetron sputtering, J. Alloys. Compd. 725 (2017) 60–68, https://doi.org/10.1016/j.jallcom.2017.07.121.

[28] H. Li, W. Duan, A. Lambertz, J. Hüpkes, K. Ding, U. Rau, O. Astakhov, Influence of room temperature sputtered Al-doped zinc oxide on passivation quality in silicon heterojunction solar cells, IEEe J. Photovolt. 9 (2019) 1485–1491, https://doi.org/10.1109/JPHOTOV.2019.2933185.

[29] K.C. Park, D.Y. Ma, K.H. Kim, The physical properties of Al-doped zinc oxide films prepared by RF magnetron sputtering, Thin Solid Films 305 (1–2) (1997) 201–209, https://doi.org/10.1016/S0040-6090(97)00215-0.

[30] H. Li, W. Duan, A. Lambertz, J. Hüpkes, K. Ding, F. Finger, U. Rau, O. Astakhov, Application of room temperature sputtered al-doped zinc oxide in silicon heterojunction solar cells, in: 2018 IEEE 7th World Conference on Photovoltaic Energy Conversion (WCPEC) (A Joint Conference of 45th IEEE PVSC, 28th PVSEC & 34th EU PVSEC), 2018, pp. 2151–2154, https://doi.org/10.1109/JPHOTOV.2019.2933185.

[31] A.B. Morales-Vilches, et al., ITO-Free silicon heterojunction solar cells with ZnO: Al/SiO2 front electrodes reaching a conversion efficiency of 23%, IEEe J. Photovolt. 9 (1) (2019) 34–39, https://doi.org/10.1109/JPHOTOV.2018.2873307. Jan.

[32] D. Meza, A. Cruz, A.B. Morales-Vilches, L. Korte, B. Stannowski, Aluminum-Doped zinc oxide as front electrode for rear emitter silicon heterojunction solar cells with high efficiency, Appl. Sci. 9 (5) (2019) 862, https://doi.org/10.3390/app9050862.

[33] L.-L. Senaud, et al., Aluminium-Doped zinc oxide rear reflectors for high-efficiency silicon heterojunction solar cells, IEEe J. Photovolt. 9 (5) (2019) 1217–1224, https://doi.org/10.1109/JPHOTOV.2019.2926860.

[34] Z. Wu, W. Duan, A. Lambertz, D. Qiu, M. Pomaska, Z. Yao, U. Rau, L. Zhang, Z. Liu, K. Ding, Low-resistivity p-type a-Si:H/AZO hole contact in high-efficiency silicon heterojunction solar cells, Appl. Surf. Sci. 542 (2021) 148749, https://doi.org/10.1016/j.apsusc.2020.148749.

[35] D.A. Muller, Structure and bonding at the atomic scale by scanning transmission electron microscopy, Nat. Mater. 8 (4) (2009) 263–270, https://doi.org/10.1038/nmat2380.

[36] L. Sagalowicz, G.R. Fox, Planar defects in ZnO thin films deposited on optical fibers and flat substrates, J. Mater. Res. 14 (5) (1999) 1876–1885, https://doi.org/10.1557/JMR.1999.0252.

[37] J. Lee, D. Lee, D. Lim, K. Yang, Structural, electrical and optical properties of ZnO: al films deposited on flexible organic substrates for solar cell applications, Thin Solid Films 515 (15) (2007) 6094–6098, https://doi.org/10.1016/j.tsf.2006.12.099.

[38] K. Omri, I. Najeh, S. Mnefgui, N. Alonizan, S. Gouadria, Microstructure, AC conductivity and complex modulus analysis of Ca-ZnO nanoparticles for potential optoelectronic applications, Mater. Sci. Eng. B 297 (2023) 116738, https://doi.org/10.1016/j.mseb.2023.116738.

[39] A.D. Darbal, M. Gemmi, J. Portillo, E. Rauch, S. Nicolopoulos, Nanoscale automated phase and orientation mapping in the TEM, Micros. Today 20 (6) (2012) 38–42, https://doi.org/10.1017/S1551929512000818.

[40] V. Coleman, C. Jagadish, Basic properties and applications of ZnO. Zinc Oxide Bulk, Thin Films and Nanostructures, Elsevier, 2005, pp. 1–20, https://doi.org/10.1016/B978-008044722-3/50001-4.

[41] S. Li, M. Pomaska, A. Lambertz, W. Duan, K. Bittkau, D. Qiu, Z. Yao, M. Luysberg, P. Steuter, M. Köhler, K. Qiu, R. Hong, H. Shen, F. Finger, T. Kirchartz, U. Rau, K. Ding, Transparent-conductive-oxide-free front contacts for high-efficiency silicon heterojunction solar cells, Joule 5 (6) (2021) 1535–1547, https://doi.org/10.1016/j.joule.2021.04.004.